

The VVDS type–1 AGN sample: The faint end of the luminosity function

A. Bongiorno¹, G. Zamorani², I. Gavignaud³, B. Marano¹, S. Paltani^{4,5}, G. Mathez⁶, J.P. Picat⁶, M. Cirasuolo⁷, F. Lamareille^{2,6}, D. Bottini⁸, B. Garilli⁸, V. Le Brun⁹, O. Le Fèvre⁹, D. Maccagni⁸, R. Scaramella^{10,11}, M. Scodreggio⁸, L. Tresse⁹, G. Vettolani¹⁰, A. Zanichelli¹⁰, C. Adami⁹, S. Arnouts⁹, S. Bardelli², M. Bolzonella², A. Cappi², S. Charlot^{12,13}, P. Ciliegi², T. Contini⁶, S. Foucaud¹⁴, P. Franzetti⁸, L. Guzzo¹⁵, O. Ilbert¹⁶, A. Iovino¹⁵, H.J. McCracken^{13,17}, C. Marinoni¹⁸, A. Mazure⁹, B. Meneux^{8,15}, R. Merighi², R. Pellò⁶, A. Pollo^{9,19}, L. Pozzetti², M. Radovich²⁰, E. Zucca², E. Hatziminaoglou²¹, M. Polletta²², M. Bondi¹⁰, J. Brinchmann²³, O. Cucciati^{15,24}, S. de la Torre⁹, L. Gregorini²⁵, Y. Mellier^{13,17}, P. Merluzzi²⁰, S. Temporin¹⁵, D. Vergani⁸, and C.J. Walcher⁹

(Affiliations can be found after the references)

Received; accepted

Abstract

In a previous paper (Gavignaud et al. 2006), we presented the type–1 Active Galactic Nuclei (AGN) sample obtained from the first epoch data of the VIMOS-VLT Deep Survey (VVDS). The sample consists of 130 faint, broad-line AGN with redshift up to $z = 5$ and $17.5 < I_{AB} < 24.0$, selected on the basis of their spectra.

In this paper we present the measurement of the Optical Luminosity Function up to $z = 3.6$ derived from this sample, we compare our results with previous results from brighter samples both at low and at high redshift.

Our data, more than one magnitude fainter than previous optical surveys, allow us to constrain the faint part of the luminosity function up to high redshift.

By combining our faint VVDS sample with the large sample of bright AGN extracted from the SDSS DR3 (Richards et al., 2006b), we find that the model which better represents the combined luminosity functions, over a wide range of redshift and luminosity, is a luminosity dependent density evolution (LDDE) model, similar to those derived from the major X-surveys. Such a parameterization allows the redshift of the AGN space density peak to change as a function of luminosity and explains the excess of faint AGN that we find at $1.0 < z < 1.5$. On the basis of this model we find, for the first time from the analysis of optically selected samples, that the peak of the AGN space density shifts significantly towards lower redshift going to lower luminosity objects. This result, already found in a number of X-ray selected samples of AGN, is consistent with a scenario of “AGN cosmic downsizing”, in which the density of more luminous AGN, possibly associated to more massive black holes, peaks earlier in the history of the Universe, than that of low luminosity ones.

Key words. surveys-galaxies: high-redshift - AGN: luminosity function

1. Introduction

Active Galactic Nuclei (AGN) are relatively rare objects that exhibit some of the most extreme physical conditions and activity known in the universe.

A useful way to statistically describe the AGN activity along the cosmic time is through the study of their luminosity function, whose shape, normalization and evolution can be used to derive constraints on models of cosmological evolution of black holes (BH). At $z \lesssim 2.5$, the luminosity function of optically selected type–1 AGN has been well studied since many years (Boyle et al., 1988; Hewett et al., 1991; Pei, 1995; Boyle et al., 2000; Croom et al., 2004). It is usually described as a double power law, characterized by the evolutionary parameters $L^*(z)$ and $\Phi^*(z)$, which allow to distinguish between simple evolutionary models such as Pure Luminosity Evolution (PLE) and Pure Density Evolution (PDE). Although the PLE and PDE models should be mainly considered as mathematical descriptions of the evolution of the luminosity function, two different physical interpretations can be associated to them: either a small

fraction of bright galaxies harbor AGN, and the luminosities of these sources change systematically with time (‘luminosity evolution’), or all bright galaxies harbor AGN, but at any given time most of them are in ‘inactive’ states. In the latter case, the fraction of galaxies with AGN in an ‘active’ state changes with time (‘density evolution’). Up to now, the PLE model is the preferred description for the evolution of optically selected QSOs, at least at low redshift ($z < 2$).

Works on high redshift type–1 AGN samples (Warren et al., 1994; Kennefick et al., 1995; Schmidt et al., 1995; Fan et al., 2001; Wolf et al., 2003; Hunt et al., 2004) have shown that the number density of QSOs declines rapidly from $z \sim 3$ to $z \sim 5$. Since the size of complete and well studied samples of QSOs at high redshift is still relatively small, the rate of this decline and the shape of the high redshift luminosity function is not yet as well constrained as at low redshift. For example, Fan et al. (2001), studying a sample of 39 luminous high redshift QSOs at $3.6 < z < 5.0$, selected from the commissioning data of the Sloan Digital Sky Survey (SDSS), found that the slope of the bright end of the QSO luminosity function evolves with redshift, becoming flatter at high redshift, and that the QSO evolution from $z = 2$ to $z = 5$ cannot be described as a pure luminosity evolution. A similar result on the flattening at high redshift of the slope of

the luminosity function for luminous QSOs has been recently obtained by Richards et al. (2006b) from the analysis of a much larger sample of SDSS QSOs (but see Fontanot et al. (2007) for different conclusions drawn on the basis of combined analysis of GOODS and SDSS QSOs).

At the same time, a growing number of observations at different redshifts, in radio, optical and soft and hard X-ray bands, are suggesting that also the faint end slope evolves, becoming flatter at high redshift (Page et al., 1997; Miyaji et al., 2000, 2001; La Franca et al., 2002; Cowie et al., 2003; Ueda et al., 2003; Fiore et al., 2003; Hunt et al., 2004; Cirasuolo et al., 2005; Hasinger et al., 2005). This evolution, now dubbed as “AGN cosmic downsizing” is described either as a direct evolution in the faint end slope or as “luminosity dependent density evolution” (LDDE), and it has been the subject of many speculations since it implies that the space density of low luminosity AGNs peaks at lower redshift than that of bright ones.

It has been observed that, in addition to the well known local scale relations between the black hole (BH) masses and the properties of their host galaxies (Kormendy & Richstone, 1995; Magorrian et al., 1998; Ferrarese & Merritt, 2000), also the galaxy spheroid population follows a similar pattern of “cosmic downsizing” (Cimatti et al., 2006). Various models have been proposed to explain this common evolutionary trend in AGN and spheroid galaxies. The majority of them propose that the feedback from the black hole growth plays a key role in determining the BH-host galaxy relations (Silk & Rees, 1998; Di Matteo et al., 2005) and the co-evolution of black holes and their host galaxies. Indeed, AGN feedback can shut down the growth of the most massive systems steepening the bright end slope (Scannapieco & Oh, 2004), while the feedback-driven QSO decay determines the shape of the faint end of the QSO LF (Hopkins et al., 2006).

This evolutionary trend has not been clearly seen yet with optically selected type-1 AGN samples. By combining results from low and high redshifts, it is clear from the studies of optically selected samples that the cosmic QSO evolution shows a strong increase of the activity from $z \sim 0$ out to $z \sim 2$, reaches a maximum around $z \simeq 2 - 3$ and then declines, but the shape of the turnover and the redshift evolution of the peak in activity as a function of luminosity is still unclear.

Most of the optically selected type-1 AGN samples studied so far are obtained through various color selections of candidates, followed by spectroscopic confirmation (e.g. 2dF, Croom et al. 2004 and SDSS, Richards et al. 2002), or grism and slitless spectroscopic surveys. These samples are expected to be highly complete, at least for luminous type-1 AGN, at either $z \leq 2.2$ or $z \geq 3.6$, where type-1 AGN show conspicuous colors in broad band color searches, but less complete in the redshift range $2.2 \leq z \leq 3.6$ (Richards et al. 2002).

An improvement in the multi-color selection in optical bands is through the simultaneous use of many broad and medium band filters as in the COMBO-17 survey (Wolf et al., 2003). This survey is the only optical survey so far which, in addition to covering a redshift range large enough to see the peak of AGN activity, is also deep enough to sample up to high redshift type-1 AGN with luminosity below the break in the luminosity function. However, only photometric redshifts are available for this sample and, because of their selection criteria, it is incomplete for objects with a small ratio between the nuclear flux and the total host galaxy flux and for AGN with anomalous colors, such as, for example, the broad absorption line (BAL) QSOs, which have on average redder colors and account for $\sim 10 - 15\%$ of the overall AGN population (Hewett & Foltz, 2003).

The VIMOS-VLT Deep Survey (Le Fèvre et al., 2005) is a spectroscopic survey in which the target selection is purely flux limited (in the I-band), with no additional selection criterion. This allows the selection of a spectroscopic type-1 AGN sample free of color and/or morphological biases in the redshift range $z > 1$. An obvious advantage of such a selection is the possibility to test the completeness of the most current surveys (see Gavignaud et al., 2006, Paper I), based on morphological and/or color pre-selection, and to study the evolution of type-1 AGN activity in a large redshift range.

In this paper we use the type-1 AGN sample selected from the VVDS to derive the luminosity function in the redshift range $1 < z < 3.6$. The VVDS type-1 AGN sample is more than one magnitude deeper than any previous optically selected sample and allow thus to explore the faint part of the luminosity function. Moreover, by combining this LF with measurement of the LF in much larger, but very shallow, surveys, we find an analytical form to describe, in a large luminosity range, the evolution of type-1 AGN in the redshift range $0 < z < 4$. The paper is organized as follows: in Section 2 and 3 we describe the sample and its color properties. In Section 4 we present the method used to derive the luminosity function, while in Section 5 we compare it with previous works both at low and high redshifts. The bolometric LF and the comparison with the results derived from samples selected in different bands (from X-ray to IR) is then presented in Section 6. The derived LF fitting models are presented in Section 7 while the AGN activity as a function of redshift is shown in Section 8. Finally in section 9 we summarize our results. Throughout this paper, unless stated otherwise, we assume a cosmology with $\Omega_m = 0.3$, $\Omega_\Lambda = 0.7$ and $H_0 = 70 \text{ km s}^{-1} \text{ Mpc}^{-1}$.

2. The sample

Our AGN sample is extracted from the first epoch data of the VIMOS-VLT Deep Survey, performed in 2002 (Le Fèvre et al., 2005).

The VVDS is a spectroscopic survey designed to measure about 150,000 redshifts of galaxies, in the redshift range $0 < z < 5$, selected, nearly randomly, from an imaging survey (which consists of observations in U, B, V, R and I bands and, in a small area, also K-band) designed for this purpose. Full details about VIMOS photometry can be found in Le Fèvre et al. (2004a), McCracken et al. (2003), Radovich et al. (2004) for the U-band and Iovino et al. (2005) for the K-band. In this work we will as well use the Galex UV-catalog (Arnouts et al., 2005; Schiminovich et al., 2005), the u^*, g', r', i', z' photometry obtained in the frame of the Canada-France-Hawaii Legacy Survey (CFHTLS)¹, UKIDSS (Lawrence et al., 2006), and the Spitzer Wide-area InfraRed Extragalactic survey (SWIRE) (Lonsdale et al., 2003, 2004). The spectroscopic VVDS survey consists of a deep and a wide survey and it is based on a simple selection function. The sample is selected only on the basis of the I band magnitude: $17.5 < I_{AB} < 22.5$ for the wide and $17.5 < I_{AB} < 24.0$ for the deep sample. For a detailed description of the spectroscopic survey strategy and the first epoch data see Le Fèvre et al. (2005).

Our sample consists of 130 AGN with $0 < z < 5$, selected in 3 VVDS fields (0226-04, 1003+01 and 2217-00) and in the Chandra Deep Field South (CDFs, Le Fèvre et al., 2004b). All of them are selected as AGN only on the basis of their spectra,

¹ www.cfht.hawaii.edu/Science/CFHLS

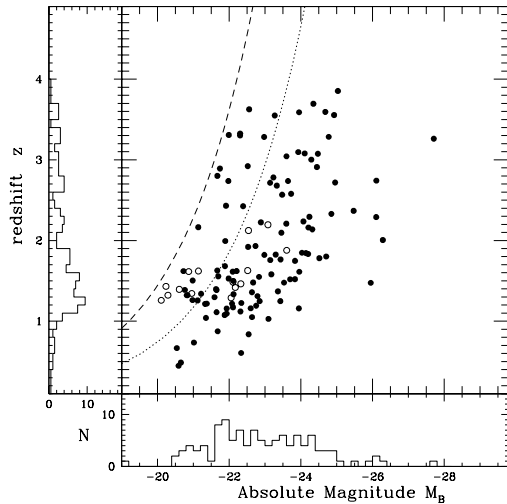


Figure 1. Distribution of absolute magnitudes and redshifts of the total AGN sample. Open circles are the objects with ambiguous redshift, shown at all their possible z values. The dotted and dashed lines represent the magnitude limits of the samples: $I_{AB} < 22.5$ for the wide sample and $I_{AB} < 24.0$ for the deep sample.

irrespective of their morphological or color properties. In particular, we selected them on the basis of the presence of at least one broad emission line. We discovered 74 of them in the deep fields (62 in the 02h field and 12 in the CDFS) and 56 in the wide fields (18 in the 10h field and 38 in the 22h field). This represents an unprecedented complete sample of faint AGN, free of morphological or color selection bias. The spectroscopic area covered by the First Epoch Data is 0.62 deg^2 in the deep fields (02h field and CDFS) and 1.1 deg^2 in the wide fields (10h and 22h fields).

To each object we have assigned a value for the spectroscopic redshift and a spectroscopic quality flag which quantifies our confidence level in that given redshift. As of today, we have 115 AGN with secure redshift, and 15 AGN with two or more possible values for the redshift. For these objects, we have two or more possible redshifts because only one broad emission line, with no other narrow lines and/or additional features, is detected in the spectral wavelength range adopted in the VVDS (5500 - 9500 Å) (see Figure 1 in Paper I). For all of them, however, a *best solution* is proposed. In the original VVDS AGN sample, the number of AGN with this redshift degeneracy was 42. To solve this problem, we have first looked for the objects already observed in other spectroscopic surveys in the same areas, solving the redshift for 3 of them. For the remaining objects, we performed a spectroscopic follow-up with FORS1 on the VLT Unit Telescope 2 (UT2). With these additional observations we found a secure redshift for 24 of our AGN with ambiguous redshift determination and, moreover, we found that our proposed best solution was the correct one in $\sim 80\%$ of the cases. On the basis of this result, we decided to use, in the following analysis, our best estimate of the redshift for the small remaining fraction of AGN with ambiguous redshift determination (15 AGN).

In Figure 1 we show the absolute B-magnitude and the redshift distributions of the sample. As shown in this Figure, our sample spans a large range of luminosities and consists of both Seyfert galaxies ($M_B > -23$; $\sim 59\%$) and QSOs ($M_B < -23$; $\sim 41\%$). A more detailed and exhaustive description of the prop-

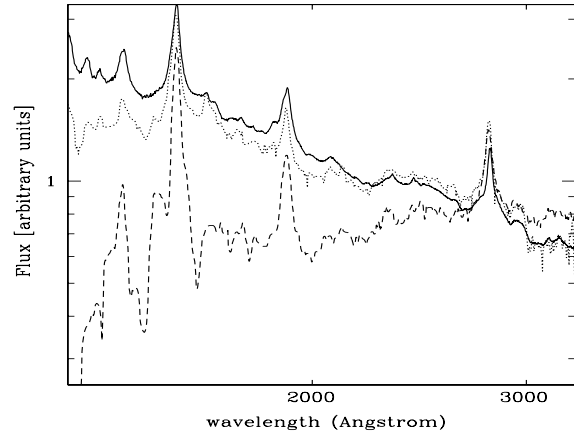


Figure 2. Composite spectra derived for our AGN with secure redshift in the 02h field, divided in a “bright” (19 objects at $M_{1450} < -22.15$, dotted curve) and a “faint” (31 objects at $M_{1450} > -22.15$, dashed curve) sample. We consider here only AGN with $z > 1$ (i.e. the AGN used in to compute the luminosity function). The SDSS composite spectrum is shown with a solid line for comparison.

erties of the AGN sample is given in Paper I (Gavignaud et al., 2006) and the complete list of BLAGN in our wide and deep samples is available as an electronic Table in Appendix of Gavignaud et al. (2006).

3. Colors of BLAGNs

As already discussed in Paper I, the VVDS AGN sample shows, on average, redder colors than those expected by comparing them, for example, with the color track derived from the SDSS composite spectrum (Vanden Berk et al., 2001). In Paper I we proposed three possible explanations: (a) the contamination of the host galaxy is reddening the observed colors of faint AGN; (b) BLAGN are intrinsically redder when they are faint; (c) the reddest colors are due to dust extinction. On the basis of the statistical properties of the sample, we concluded that hypothesis (a) was likely to be the more correct, as expected from the faint absolute magnitudes sampled by our survey, even if hypotheses (b) and (c) could not be ruled out.

In Figure 2 we show the composite spectra derived from the sample of AGN with secure redshift in the 02h field, divided in a “bright” and a “faint” sample at the absolute magnitude $M_{1450} = -22.15$. We consider here only AGN with $z > 1$, which correspond to the AGN used in Section 4 to compute the luminosity function. The choice of the reference wavelength for the absolute magnitude, $\lambda = 1450 \text{ Å}$, is motivated by our photometric coverage. In fact, for most of the objects it is possible to interpolate M_{1450} directly from the observed magnitudes. In the same plot we show also the SDSS composite spectrum (solid curve) for comparison. Even if also the “bright” VVDS composite (dotted curve) is somewhat redder than the SDSS one, it is clear from this plot that the main differences occur for faintest objects (dashed curve).

A similar result is shown for the same sample in the upper panel of Figure 3, where we plot the spectral index α as a function of the AGN luminosity. The spectral index is derived here by fitting a simple power law $f(\nu) = \nu^{-\alpha}$ to our photometric data points. This analysis has been performed only on the 02h deep

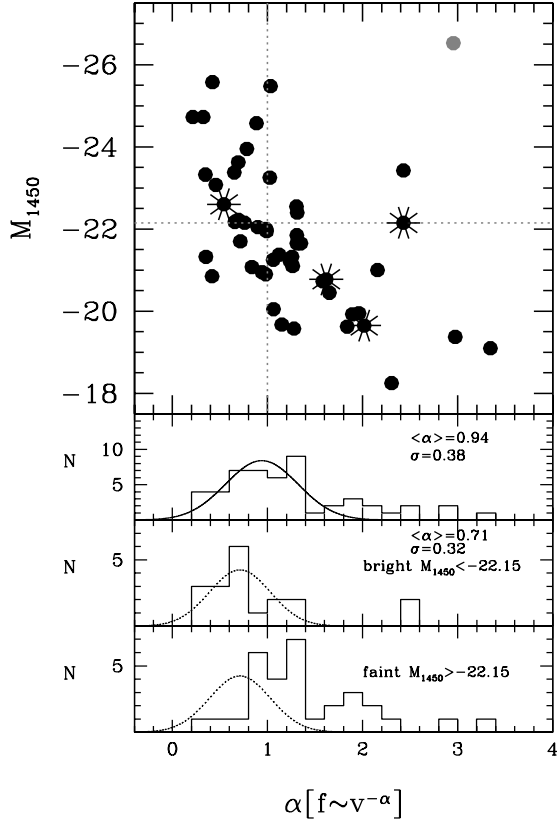


Figure 3. *Upper Panel:* Distribution of the spectral index α as a function of M_{1450} for the same sample of AGN as in Figure 2. The spectral index is derived here by fitting a simple power law $f(\nu) = \nu^{-\alpha}$ to our photometric data points. Asterisks are AGN morphologically classified as extended and the grey point is a BAL AGN. *Bottom Panels:* Distribution of the spectral index α for the same sample of AGN. All the AGN in this sample are shown in the first of the three panels, while the AGN in the “bright” and “faint” sub-samples are shown in the second and third panel, respectively. The dotted curve in the second panel corresponds to the gaussian fit of the bright sub-sample and it is reported also in the third panel to highlight the differences in the α distributions of the two sub-samples.

sample, since for the wide sample we do not have enough photometric coverage to reliably derive the spectral index. Most of the AGN with $\alpha > 1$ are fainter than $M_{1450} = -22.15$, showing that, indeed, the faintest objects have on average redder colors than the brightest ones. The outlier (the brightest object with large α , i.e. very red colors, in the upper right corner of the plot) is a BAL AGN.

The three bottom panels of Figure 3 show the histograms of the resulting power law slopes for the same AGN sample. The total sample is plotted in the first panel, while the bright and the faint sub-samples are plotted in the second and third panels, respectively. A Gaussian curve with $\langle \alpha \rangle = 0.94$ and dispersion $\sigma = 0.38$ is a good representation for the distribution of about 80% (40/50) of the objects in the first panel. In addition, there is a significant tail ($\sim 20\%$) of redder AGN with slopes in the range from 1.8 up to ~ 3.0 . The average slope of the total sample (~ 0.94) is redder than the fit to the SDSS composite (~ 0.44). Moreover, the distribution of α is shifted toward much larger val-

ues (redder continua) than the similar distribution in the SDSS sample (Richards et al., 2003). For example, only 6% of the objects in the SDSS sample have $\alpha > 1.0$, while this percentage is 57% in our sample.

The differences with respect to the SDSS sample can be partly due to the differences in absolute magnitude of the two samples ($M_i < -22.0$ for the SDSS sample (Schneider et al., 2003) and $M_B < -20.0$ for the VVDS sample). In fact, if we consider the VVDS “bright” sub-sample, the average spectral index $\langle \alpha \rangle$ becomes ~ 0.71 , which is closer to the SDSS value (even if it is still somewhat redder), and only two objects ($\sim 8\%$ of the sample) show values not consistent with a gaussian distribution with $\sigma \sim 0.32$. Moreover, only 30% of this sample have $\alpha > 1.0$.

Most of the bright SDSS AGNs with $\alpha > 1$ are interpreted by Richards et al. (2003) to be dust-reddened, although a fraction of them is likely to be due to intrinsically red AGN (Hall et al., 2006). At fainter magnitude one would expect both a larger fraction of dust-reddened objects (in analogy with indications from the X-ray data (Brandt et al., 2000; Mushotzky et al., 2000) and a more significant contamination from the host galaxy.

We have tested these possibilities by examining the global Spectral Energy Distribution (SED) of each object and fitting the observed fluxes f_{obs} with a combination of AGN and galaxy emission, allowing also for the possibility of extinction of the AGN flux. Thanks to the multi-wavelength coverage in the deep field in which we have, in addition to VVDS bands, also data from GALEX, CFHTLS, UKIDSS and SWIRE, we can study the spectral energy distribution of the single objects. In particular, we assume that:

$$f_{obs} = c_1 f_{AGN} \cdot 10^{-0.4 A_\lambda} + c_2 f_{GAL} \quad (1)$$

and, using a library of galaxy and AGN templates, we find the best parameters c_1 , c_2 and E_{B-V} for each object. We used the AGN SED derived by Richards et al. (2006a) with an SMC-like dust-reddening law (Prevot et al., 1984) with the form $A_\lambda/E_{B-V} = 1.39 \lambda_{\mu m}^{-1.2}$, and a library of galaxies template by Bruzual & Charlot (2003).

We found that for $\sim 37\%$ of the objects, the observed flux is fitted by a typical AGN power law (pure AGN), while 44% of the sources require the presence of a contribution from the host galaxy to reproduce the observed flux. Only 4% of the objects are fitted by pure AGN + dust, while the remaining 15% of objects require instead both contributions (host galaxy contamination and presence of dust). As expected, if we restrict the analysis to the bright sample, the percentage of pure AGN increases to 68%, with the rest of the objects requiring either some contribution from the host galaxy ($\sim 21\%$) or the presence of dust obscuration ($\sim 11\%$).

In Figure 4 we show 4 examples of the resulting fits: (i) pure AGN; (ii) dust-extinguished AGN; (iii) AGN contaminated by the host galaxy; (iv) dust-extinguished AGN and contaminated by the host galaxy. The dotted line corresponds to the AGN template before applying the extinction law, while the solid blue line corresponds to the same template, but extinguished for the given E_{B-V} ; the red line corresponds to the galaxy template and, finally, the black line is the resulting best fit to the SED. The host galaxy contaminations will be taken into account in the computation of the AGN absolute magnitude for the luminosity function.

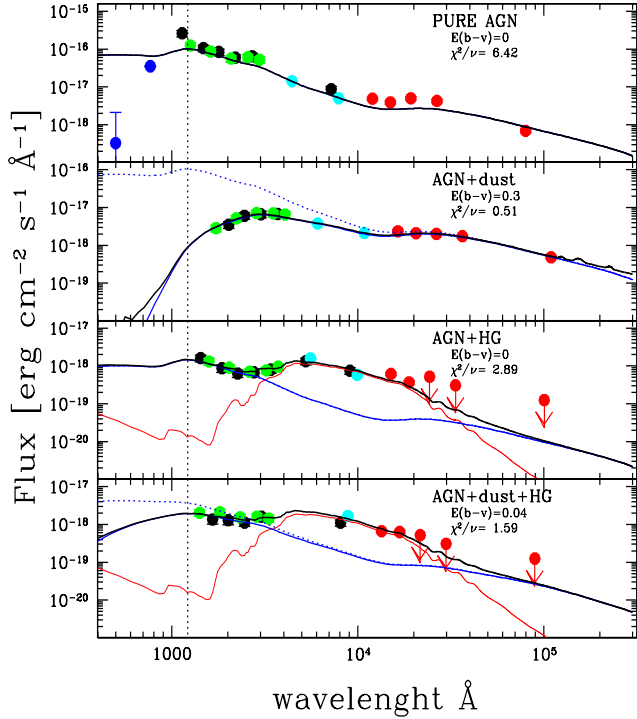


Figure 4. Four examples of different decompositions of the observed SEDs of our objects. Since for $\lambda < 1216 \text{ \AA}$, corresponding to the Ly α line, the observed flux is expected to decrease because of intervening absorption, all the photometric data at $\lambda < 1216 \text{ \AA}$ are not considered in the fitting. The only requested constraint is that they lie below the fit. The four fits shown in this Figure correspond, from top to bottom, to pure-AGN, dust-extinguished AGN, AGN and host galaxy, dust-extinguished AGN and host galaxy. The dotted line corresponds to the AGN template before applying the extinction law, while the solid blue line corresponds to the same template, but extinguished for the given E_{B-V} . The red line (third and fourth panel) corresponds to the galaxy template and, finally, the black line is the resulting best fit to the SED. Arrows correspond to 5σ upper limits in case of non detection in the IR.

4. Luminosity function

4.1. Definition of the redshift range

For the study of the LF we decided to exclude AGN with $z \leq 1.0$. This choice is due to the fact that for $0.5 \leq z \leq 1.0$ the only visible broad line in the VVDS spectra is H β (see Figure 1 of Paper I). This means that all objects with narrow or almost narrow H β and broad H α (type 1.8, 1.9 AGN; see Osterbrock 1981) would not be included in our sample, because we include in the AGN sample all the objects with at least one visible broad line. Since at low luminosities the number of intermediate type AGN is not negligible, this redshift bin is likely to be underpopulated and the results would not be meaningful.

At $z < 0.5$, in principle we have less problems, because also H α is within the wavelength range of the VVDS spectra, but, since at this low redshift, our sampled volume is relatively small and QSOs rare, only 3 objects have secure redshifts in this redshift bin in the current sample. For these reasons, our luminosity function has been computed only for $z > 1.0$ AGN. As already mentioned in Section 2, the small fraction of objects with an am-

biguous redshift determination have been included in the computation of the luminosity function assuming that our best estimate of their redshift is correct.

The resulting sample used in the computation of the LF consists thus of 121 objects at $1 < z < 4$.

4.2. Incompleteness function

Our incompleteness function is made up of two terms linked, respectively, to the selection algorithm and to the spectral analysis: the Target Sampling Rate (TSR) and the Spectroscopic Success Rate (SSR) defined following Ilbert et al. (2005).

The Target Sampling Rate, namely the ratio between the observed sources and the total number of objects in the photometric catalog, quantifies the incompleteness due to the adopted spectroscopic selection criterion. The TSR is similar in the wide and deep sample and runs from 20% to 30%.

The Spectroscopic Success Rate is the probability of a spectroscopically targeted object to be securely identified. It is a complex function of the BLAGN redshift, apparent magnitude and intrinsic spectral energy distribution and it has been estimated by simulating 20 Vimos pointings, for a total of 2745 spectra.

Full details on TSR and SSR can be found in Paper I (Gavignaud et al., 2006). We account for them by computing for each object the associated weights $w^{TSR} = 1/TSR$ and $w^{SSR} = 1/SSR$; the total weighted contribution of each object to the luminosity function is then the product of the derived weights ($w^{TSR} \times w^{SSR}$).

4.3. Estimate of the absolute magnitude

We derived the absolute magnitude in the reference band from the apparent magnitude in the observed band as:

$$M = m_{obs} - 5 \log_{10}(dl(z)) - 25 - k \quad (2)$$

where M is computed in the band in which we want to compute the luminosity function, m_{obs} is the observed band from which we want to calculate it, $dl(z)$ is the luminosity distance expressed in Mpc and k is the k -correction in the reference band. To make easier the comparison with previous results in the literature, we computed the luminosity function in the B-band.

To minimize the uncertainties in the adopted k -correction, m_{obs} for each object should be chosen in the observed band which is sampling the rest-wavelength closer to the band in which the luminosity function is computed. For our sample, which consists only of $z > 1$ objects, the best bands to use to compute the B-band absolute magnitudes should be respectively the I-, J- and K-bands going to higher redshift. Since however, the only observed band available for the entire sample (deep and wide), is the I-band, we decided to use it for all objects to compute the B-band magnitudes. This means that for $z \gtrsim 2$, we introduce an uncertainty in the absolute magnitudes due to the k -correction. We computed the absolute magnitude considering the template derived from the SDSS sample (Vanden Berk et al., 2001).

As discussed in Section 3, the VVDS AGN sample shows redder colors than those typical of normal, more luminous AGN and this can be due to the combination of the host galaxy contribution and the presence of dust. Since, in this redshift range, the fractional contribution from the host galaxies is expected to be more significant in the I-band than in bluer bands, the luminosity derived using the I-band observed magnitude could, in some cases, be somewhat overestimated due to the contribution of the host galaxy component.

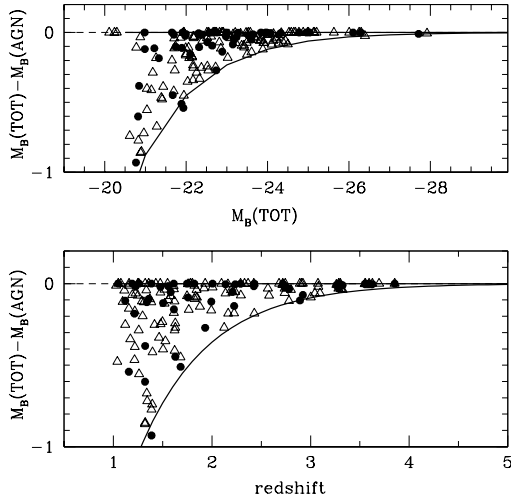


Figure 5. Real (full circles; AGN in the deep sample) and simulated (open triangles; AGN in the wide sample) B-band absolute magnitude differences as a function of $M_B(\text{TOT})$ (upper panel) and redshift (bottom panel). $M_B(\text{TOT})$ is the absolute magnitude computed considering the total observed flux, while $M_B(\text{AGN})$ is the absolute magnitude computed after subtracting the host-galaxy contribution.

We estimated the possible impact of this effect on our results in the following way. From the results of the analysis of the SED of the single objects in the deep sample (see Section 3) we computed for each object the difference $m_I(\text{TOT}) - m_I(\text{AGN})$ and, consequently, $M_B(\text{TOT}) - M_B(\text{AGN})$. This could allow us to derive the LF using directly the derived $M_B(\text{AGN})$, resolving the possible bias introduced by the host galaxy contamination. These differences are shown as full circles in Figure 5 as a function of absolute magnitude (upper panel) and redshift (lower panel). For most of the objects the resulting differences between the total and the AGN magnitudes are small ($\Delta M \leq 0.2$). However, for a not negligible fraction of the faintest objects ($M_B \geq -22.5$, $z \leq 2.0$) these differences can be significant (up to ~ 1 mag). For the wide sample, for which the more restricted photometric coverage does not allow a detailed SED analysis and decomposition, we used simulated differences to derive the $M_B(\text{AGN})$. These simulated differences have been derived through a Monte Carlo simulation on the basis of the bivariate distribution $\Delta M(M, z)$ estimated from the objects in the deep sample. $\Delta M(M, z)$ takes into account the probability distribution of ΔM as a function of M_B and z , between 0 and the solid line in Figure 5 derived as the envelope suggested by the black dots. The resulting simulated differences for the objects in the wide sample are shown as open triangles in the two panels of Figure 5.

The AGN magnitudes and the limiting magnitudes of the samples have been corrected also for galactic extinction on the basis of the mean extinction values $E(B-V)$ in each field derived from Schlegel et al. (1998). Only for the 22h field, where the extinction is highly variable across the field, we used the extinction on the basis of the position of individual objects. The resulting corrections in the I-band magnitude are $A_I \approx 0.027$ in the 2h and 10h fields and $A_I = 0.0089$ in the CDFS field, while the average value in the 22h field is $A_I = 0.065$. These corrections have been applied also to the limiting magnitude of each field.

4.4. The $1/V_{\text{max}}$ estimator

We derived the binned representation of the luminosity function using the usual $1/V_{\text{max}}$ estimator (Schmidt, 1968), which gives the space density contribution of individual objects. The luminosity function, for each redshift bin ($z - \Delta z/2$; $z + \Delta z/2$), is then computed as:

$$\Phi(M) = \frac{1}{\Delta M} \sum_{M-\Delta M/2}^{M+\Delta M/2} \frac{w_i^{\text{TSR}} w_i^{\text{SSR}}}{V_{\text{max},i}} \quad (3)$$

where $V_{\text{max},i}$ is the comoving volume within which the i^{th} object would still be included in the sample. w_i^{TSR} and w_i^{SSR} are respectively the inverse of the TSR and of the SSR, associated to the i^{th} object. The statistical uncertainty on $\Phi(M)$ is given by Marshall et al. (1983):

$$\sigma_\phi = \frac{1}{\Delta M} \sqrt{\sum_{M-\Delta M/2}^{M+\Delta M/2} \frac{(w_i^{\text{TSR}} w_i^{\text{SSR}})^2}{V_{\text{max},i}^2}} \quad (4)$$

We combined our samples at different depths using the method proposed by Avni & Bahcall (1980). In this method it is assumed that each object, characterized by an observed redshift z_i and intrinsic luminosity L_i , could have been found in any of the survey areas for which its observed magnitude is brighter than the corresponding flux limit. This means that, for our total sample, we consider an area of:

$$\Omega_{\text{tot}}(m) = \Omega_{\text{deep}} + \Omega_{\text{wide}} = 1.72 \text{ deg}^2 \quad \text{for } 17.5 < I_{\text{AB}} < 22.5$$

and

$$\Omega_{\text{rot}}(m) = \Omega_{\text{deep}} = 0.62 \text{ deg}^2 \quad \text{for } 22.5 < I_{\text{AB}} < 24.0$$

The resulting luminosity functions in different redshift ranges are plotted in Figure 6 and 7, where all bins which contain at least one object are plotted. The LF values, together with their 1σ errors and the numbers of objects in each absolute magnitude bin are presented in Table 1. The values reported in Table 1 and plotted in Figures 6 and 7 are not corrected for the host galaxy contribution. We have in fact a posteriori verified that, even if the differences between the total absolute magnitudes and the magnitudes corrected for the host galaxy contribution (see Section 4.3) can be significant for a fraction of the faintest objects, the resulting luminosity functions computed by using these two sets of absolute magnitudes are not significantly different. For this reason and for a more direct comparison with previous works, the results on the luminosity function presented in the next section are those obtained using the total magnitudes.

5. Comparison with the results from other optical surveys

We derived the luminosity function in the redshift range $1.0 < z < 3.6$ and we compared it with the results from other surveys at both low and high redshift.

5.1. The low redshift luminosity function

In Figure 6 we present our luminosity function up to $z = 2.1$. The Figure show our LF data points (full circles) derived in two redshift bins: $1.0 < z < 1.55$ and $1.55 < z < 2.1$ compared with the LF fits derived from the 2dF QSO sample by Croom et al. (2004) and by Boyle et al. (2000), with the COMBO-17 sample

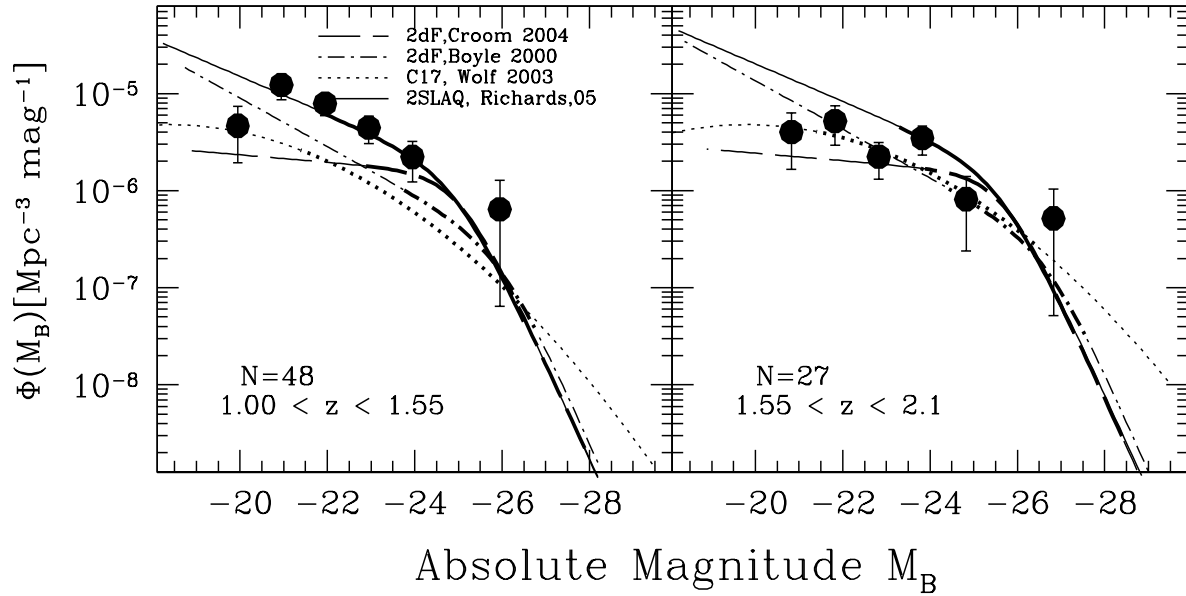


Figure 6. Our rest-frame B-band luminosity function, derived in the redshift bins $1.0 < z < 1.55$ and $1.55 < z < 2.1$, compared with the 2dFQRS (Croom et al., 2004; Boyle et al., 2000), COMBO-17 data (Wolf et al., 2003) and with the 2dF-SDSS (2SLAQ) data (Richards et al., 2005). The curves in the Figure show the PLE fit models derived by these authors. The thick parts of the curves correspond to the luminosity range covered by the data in each sample, while the thin parts are extrapolations based on the best fit parameters of the models.

by Wolf et al. (2003), and with the 2dF-SDSS (2SLAQ) LF fit by Richards et al. (2005). In each panel the curves, computed for the average z of the redshift range, correspond to a double power law luminosity function in which the evolution with redshift is characterized by a pure luminosity evolution modeled as $M_b^*(z) = M_b^*(0) - 2.5(k_1z + k_2z^2)$. Moreover, the thick parts of the curves show the luminosity range covered by the data in each of the comparison samples, while the thin parts are extrapolation based on the the best fit parameters of the models.

We start considering the comparison with the 2dF and the COMBO-17 LF fits. As shown in Figure 6, our bright LF data points connect rather smoothly to the faint part of the 2dF data. However, our sample is more than two magnitudes deeper than the 2dF sample. For this reason, a comparison at low luminosity is possible only with the extrapolations of the LF fit. At $z > 1.55$, while the Boyle’s model fits well our faint LF data points, the Croom’s extrapolation, being very flat, tends to underestimate our low luminosity data points. At $z < 1.55$ the comparison is worse: as in the higher redshift bin, the Boyle’s model fits our data better than the Croom’s one but, in this redshift bin, our data points show an excess at low luminosity also with respect to Boyle’s fit. This trend is similar to what shown also by the comparison with the fit of the COMBO-17 data which, differently from the 2dF data, have a low luminosity limit closer to ours: at $z > 1.55$ the agreement is very good, but in the first redshift bin our data show again an excess at low luminosity. This excess is likely due to the fact that, because of its selection criteria, the COMBO-17 sample is expected to be significantly incomplete for objects in which the ratio between the nuclear flux and the total host galaxy flux is small. Finally, we compare our data with the 2SLAQ fits derived by Richards et al. (2005). The 2SLAQ data are derived from a sample of AGN selected from the SDSS,

at $18.0 < g < 21.85$ and $z < 3$, and observed with the 2-degree field instrument. Similarly to the 2dF sample, also for this sample the LF is derived only for $z < 2.1$ and $M_B < -22.5$. The plotted dot-dashed curve corresponds to a PLE model in which they fixed most of the parameters of the model at the values found by Croom et al. (2004), leaving to vary only the faint end slope and the normalization constant Φ^* . In this case, the agreement with our data points at $z < 1.55$ is very good also at low luminosity. The faint end slope found in this case is $\beta = -1.45$, which is similar to that found by Boyle et al. (2000) ($\beta = -1.58$) and significantly steeper than that found by Croom et al. (2004) ($\beta = -1.09$). At $z > 1.55$, the Richards et al. (2005) LF fit tends to overestimate our data points at the faint end of the LF, which suggest a flatter slope in this redshift bin.

The first conclusion from this comparison is that, at low redshift (i.e. $z < 2.1$), the data from our sample, which is ~ 2 mag fainter than the previous spectroscopically confirmed samples, are not well fitted simultaneously in the two analyzed redshift bins by the PLE models derived from the previous samples. Qualitatively, the main reason for this appears to be the fact that our data suggest a change in the faint end slope of the LF, which appears to flatten with increasing redshift. This trend, already highlighted by previous X-ray surveys (La Franca et al., 2002; Ueda et al., 2003; Fiore et al., 2003) suggests that a simple PLE parameterization may not be a good representation of the evolution of the AGN luminosity function over a wide range of redshift and luminosity. Different model fits will be discussed in Section 7.

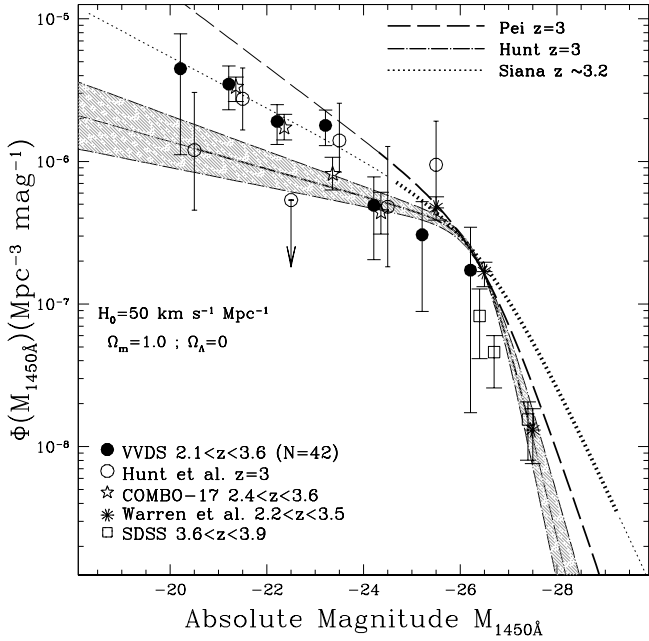


Figure 7. Our luminosity function, at 1450 Å rest-frame, in the redshift range $2.1 < z < 3.6$, compared with data from other high- z samples (Hunt et al. (2004) at $z = 3$; Combo-17 data from Wolf et al. (2003) at $2.4 < z < 3.6$; data from Warren et al. (1994) at $2.2 < z < 3.5$ and the SDSS data from Fan et al. (2001)). The SDSS data points at $3.6 < z < 3.9$ have been evolved to $z=3$ using the luminosity evolution of Pei (1995) as in Hunt et al. (2004). The curves show some model fits in which the thick parts of the curves correspond to the luminosity range covered by the data samples, while the thin parts are model extrapolation. For this plot, an $\Omega_m = 1$, $\Omega_\Lambda = 0$, $h = 0.5$ cosmology has been assumed for comparison with the previous works.

5.2. The high redshift luminosity function

The comparison of our LF data points for $2.1 < z < 3.6$ (full circles) with the results from other samples in similar redshift ranges is shown in Figure 7. In this Figure an $\Omega_m = 1$, $\Omega_\Lambda = 0$, $h = 0.5$ cosmology has been assumed for comparison with previous works, and the absolute magnitude has been computed at 1450 Å. As before, the thick parts of the curves show the luminosity ranges covered by the various data samples, while the thin parts are model extrapolations. In terms of number of objects, depth and covered area, the only sample comparable to ours is the COMBO-17 sample (Wolf et al., 2003), which, in this redshift range, consists of 60 AGN candidates over 0.78 square degree. At a similar depth, in terms of absolute magnitude, we show also the data from the sample of Hunt et al. (2004), which however consists of 11 AGN in the redshift range $\langle z \rangle \pm \sigma_z = 3.03 \pm 0.35$ (Steidel et al., 2002). Given the small number of objects, the corresponding Hunt model fit was derived including also the Warren data points (Warren et al., 1994). Moreover, they assumed the Pei (1995) luminosity evolution model, adopting the same values for L^* and Φ^* , leaving free to vary the two slopes, both at the faint and at the bright end of the LF. For comparison we show also the original Pei model fit derived from the empirical luminosity function estimated by Hartwick & Schade (1990) and Warren et al. (1994). In the

same plot we show also the model fit derived from a sample of ~ 100 $z \sim 3$ (U-dropout) QSO candidates by Siana et al. (private communication; see also Siana et al. 2006). This sample has been selected by using a simple optical/IR photometric selection at $19 < r' < 22$ and the model fit has been derived by fixing the bright end slope at $z = -2.85$ as determined by SDSS data (Richards et al., 2006b).

In general, the comparison of the VVDS data points with those from the other surveys shown in Figure 7 shows a satisfactory agreement in the region of overlapping magnitudes. The best model fit which reproduce our LF data points at $z \sim 3$ is the Siana model with a faint end slope $\beta = -1.45$. It is interesting to note that, in the faint part of the LF, our data points appear to be higher with respect to the Hunt et al. (2004) fit and are instead closer to the extrapolation of the original Pei model fit. This difference with the Hunt et al. (2004) fit is probably due to the fact that, having only 11 AGN in their faint sample, their best fit to the faint-end slope was poorly constrained.

6. The bolometric luminosity function

The comparison between the AGN LFs derived from samples selected in different bands has been for a long time a critical point in the studies of the AGN luminosity function. Recently, Hopkins et al. (2007), combining a large number of LF measurements obtained in different redshift ranges, observed wavelength bands and luminosity intervals, derived the Bolometric QSO Luminosity Function in the redshift range $z = 0 - 6$. For each observational band, they derived appropriate bolometric corrections, taking into account the variation with luminosity of both the average absorption properties (e.g. the QSO column density N_H from X-ray data) and the average global spectral energy distributions. They show that, with these bolometric corrections, it is possible to find a good agreement between results from all different sets of data.

We applied to our LF data points the bolometric corrections given by Eqs. (2) and (4) of Hopkins et al. (2007) for the B-band and we derived the bolometric LF shown as black dots in Figure 8. The solid line represents the bolometric LF best fit model derived by Hopkins et al. (2007) and the colored data points correspond to different samples: green points are from optical LFs, blue and red points are from soft-X and hard-X LFs, respectively, and finally the cyan points are from the mid-IR LFs. All these bolometric LFs data points have been derived following the same procedure described in Hopkins et al. (2007).

Our data, which sample the faint part of the bolometric luminosity function better than all previous optically selected samples, are in good agreement with all the other samples, selected in different bands. Only in the last redshift bin, our data are quite higher with respect to the samples selected in other wavelength bands. The agreement remains however good with the COMBO-17 sample which is the only optically selected sample plotted here. This effect can be attributed to the fact that the conversions used to compute the Bolometric LF, being derived especially for AGN at low redshifts, become less accurate at high redshift.

Our data show moreover good agreement also with the model fit derived by Hopkins et al. (2007). By trying various analytic fits to the bolometric luminosity function Hopkins et al. (2007) concluded that neither pure luminosity nor pure density evolution represent well all the data. An improved fit can instead be obtained with a luminosity dependent density evolution model (LDDE) or, even better, with a PLE model in which both the bright- and the faint-end slopes evolve with redshift. Both

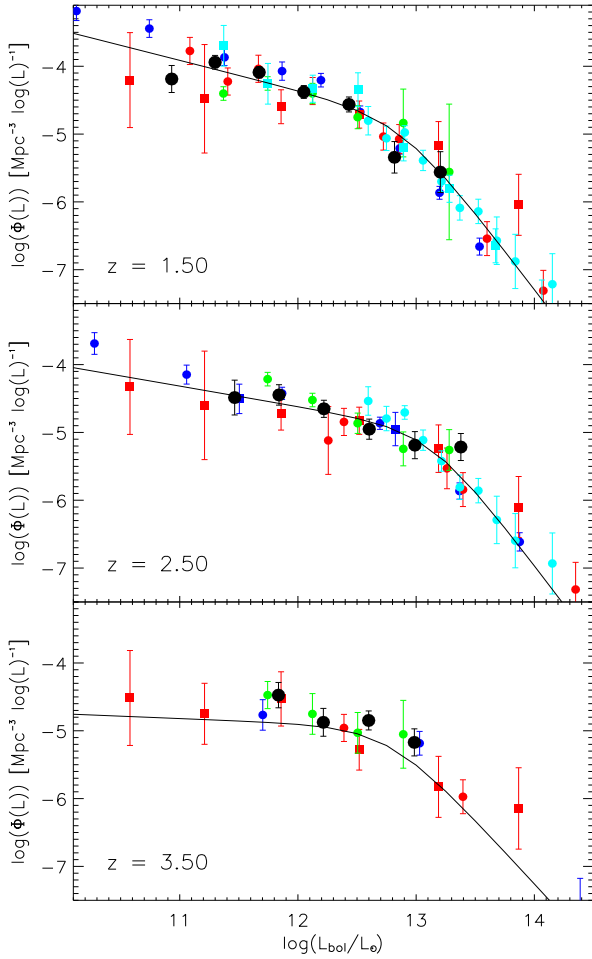


Figure 8. Bolometric luminosity function derived in three redshift bins from our data (black dots), compared with Hopkins et al. (2007) best-fit model and the data-sets used in their work. The central redshift of each bin is indicated in each panel. Here, we adopted the same color-code as in Hopkins et al. (2007), but for more clarity we limited the number of samples presented in the Figure. Red symbols correspond to hard X-ray surveys (squares: Barger et al. 2005; circles: Ueda et al. 2003). Blue to soft X-ray surveys (squares: Silverman et al. 2005; circles: Hasinger et al. 2005). Cyan to infra-red surveys (circles: Brown et al. 2006; squares: Matute et al. 2006). For the optical surveys we are showing here, with green circles, the data from the COMBO-17 survey (Wolf et al., 2003), which is comparable in depth to our sample.

these models can reproduce the observed flattening with redshift of the faint end of the luminosity function.

7. Model fitting

In this Section we discuss the results of a number of different fits to our data as a function of luminosity and redshift. For this purpose, we computed the luminosity function in 5 redshift bins at $1.0 < z < 4.0$ where the VVDS AGN sample consists of 121 objects. Since, in this redshift range, our data cover only the faint part of the luminosity function, these fits have been performed by combining our data with the LF data points from the SDSS data release 3 (DR3) (Richards et al., 2006b) in the red-

shift range $0 < z < 4$. The advantage of using the SDSS sample, rather than, for example, the 2dF sample, is that the former sample, because of the way it is selected, probes the luminosity function to much higher redshifts. The SDSS sample contains more than 15,000 spectroscopically confirmed AGN selected from an effective area of 1622 sq.deg. Its limiting magnitude ($i < 19.1$ for $z < 3.0$ and $i < 20.2$ for $z > 3.0$) is much brighter than the VVDS and because of this it does not sample well the AGN in the faint part of the luminosity function. For this reason, Richards et al. (2006b) fitted the SDSS data using only a single power law, which is meant to describe the luminosity function above the break luminosity. Adding the VVDS data, which instead mainly sample the faint end of the luminosity function, and analyzing the two samples together, allows us to cover the entire luminosity range in the common redshift range ($1.0 < z < 4.0$), also extending the analysis at $z < 1.0$ where only SDSS data are available.

The goodness of fit between the computed LF data points and the various models is then determined by the χ^2 test.

For all the analyzed models we have parameterized the luminosity function as a double power law that, expressed in luminosity, is given by:

$$\Phi(L, z) = \frac{\Phi_L^*}{(L/L^*)^{-\alpha} + (L/L^*)^{-\beta}} \quad (5)$$

where Φ_L^* is the number of AGN per Mpc^3 , L^* is the characteristic luminosity around which the slope of the luminosity function is changing and α and β are the two power law indices. Equation 5 can be expressed in absolute magnitude² as:

$$\Phi(M, z) = \frac{\Phi_M^*}{10^{0.4(\alpha+1)(M-M^*)} + 10^{0.4(\beta+1)(M-M^*)}} \quad (6)$$

7.1. The PLE and PDE models

The first model that we tested is a Pure Luminosity Evolution (PLE) with the dependence of the characteristic luminosity described by a 2nd-order polynomial in redshift:

$$M^*(z) = M^*(0) - 2.5(k_1z + k_2z^2). \quad (7)$$

Following the finding by Richards et al. (2006b) for the SDSS sample, we have allowed a change (flattening with redshift) of the bright end slope according to a linear evolution in redshift: $\alpha(z) = \alpha(0) + A z$. The resulting best fit parameters are listed in the first line of Table 2 and the resulting model fit is shown as a green short dashed line in Figure 9. The bright end slope α derived by our fit ($\alpha_{VVDS} = -3.19$ at $z = 2.45$) is consistent with the one found by Richards et al. (2006b) ($\alpha_{SDSS} = -3.1$).³

This model, as shown in Figure 9, while reproduces well the bright part of the LF in the entire redshift range, does not fit the faint part of the LF at low redshift ($1.0 < z < 1.5$). This appears to be due to the fact that, given the overall best fit normalization, the derived faint end slope ($\beta = -1.38$) is too shallow to reproduce the VVDS data in this redshift range.

Richards et al. (2005), working on a combined 2dF-SDSS (2SLAQ) sample of AGN up to $z = 2.1$. found that, fixing all of the parameters except β and the normalization, to those of Croom et al. (2004), the resulting faint end slope is $\beta = -1.45 \pm 0.03$. This value would describe better our faint LF at low redshift. This trend suggests a kind of combined luminosity and density evolution not taken into account by the used model.

² $\Phi_M^* = \Phi_L^* L^* \cdot |\ln 10^{-0.4}|$

³ in their parameterization $A_1 = -0.4(\alpha + 1) = 0.84$

For this reason, we attempted to fit the data also including a term of density evolution in the form of:

$$\Phi_M^*(z) = \Phi_M^*(0) \cdot 10^{k_1 D z + k_2 D z^2} \quad (8)$$

In this model the evolution of the LF is described by both a term of luminosity evolution, which affects M^* , and a term of density evolution, which allows for a change in the global normalization Φ^* . The derived best fit parameters of this model are listed in the second line of Table 2 and the model fit is shown as a blue long dashed line in Figure 9. This model gives a better χ^2 with respect to the previous model, describing the entire sample better than a simple PLE (the reduced χ^2 decreases from ~ 1.9 to ~ 1.35). However, it still does not satisfactorily reproduce the excess of faint objects in the redshift bin $1.0 < z < 1.5$ and, moreover, it underestimates the faint end of the LF in the last redshift bin ($3.0 < z < 4.0$).

7.2. The LDDE model

Recently, a growing number of observations at different redshifts, in soft and hard X-ray bands, have found evidences of a flattening of the faint end slope of the LF towards high redshift. This trend has been described through a luminosity-dependent density evolution parameterization. Such a parameterization allows the redshift of the AGN density peak to change as a function of luminosity. This could help in explaining the excess of faint AGN found in the VVDS sample at $1.0 < z < 1.5$. Therefore, we considered a luminosity dependent density evolution model (LDDE), as computed in the major X-surveys (Miyaji et al. 2000; Ueda et al. 2003; Hasinger et al. 2005). In particular, following Hasinger et al. (2005), we assumed an LDDE evolution of the form:

$$\Phi(M_B, z) = \Phi(M, 0) * e_d(z, M_B) \quad (9)$$

where:

$$e_d(z, M_B) = \begin{cases} (1+z)^{p_1} & (z \leq z_c) \\ e_d(z_c)[(1+z)/(1+z_c)]^{p_2} & (z > z_c) \end{cases} \quad (10)$$

along with

$$z_c(M_B) = \begin{cases} z_{c,0} 10^{-0.4\gamma(M_B - M_c)} & (M_B \geq M_c) \\ z_{c,0} & (M_B < M_c) \end{cases} \quad (11)$$

where z_c corresponds to the redshift at which the evolution changes. Note that z_c is not constant but it depends on the luminosity. This dependence allows different evolutions at different luminosities and can indeed reproduce the differential AGN evolution as a function of luminosity, thus modifying the shape of the luminosity function as a function of redshift. We also considered two different assumptions for p_1 and p_2 : (i) both parameters constant and (ii) both linearly depending on luminosity as follows:

$$p1(M_B) = p1_{M_{\text{ref}}} - 0.4\epsilon_1 (M_B - M_{\text{ref}}) \quad (12)$$

$$p2(M_B) = p2_{M_{\text{ref}}} - 0.4\epsilon_2 (M_B - M_{\text{ref}}) \quad (13)$$

The corresponding χ^2 values for the two above cases are respectively $\chi^2=64.6$ and $\chi^2=56.8$. Given the relatively small improvement of the fit, we considered the addition of the two further parameters (ϵ_1 and ϵ_2) unnecessary. The model with constant p_1 and p_2 values is shown with a solid black line in Figure

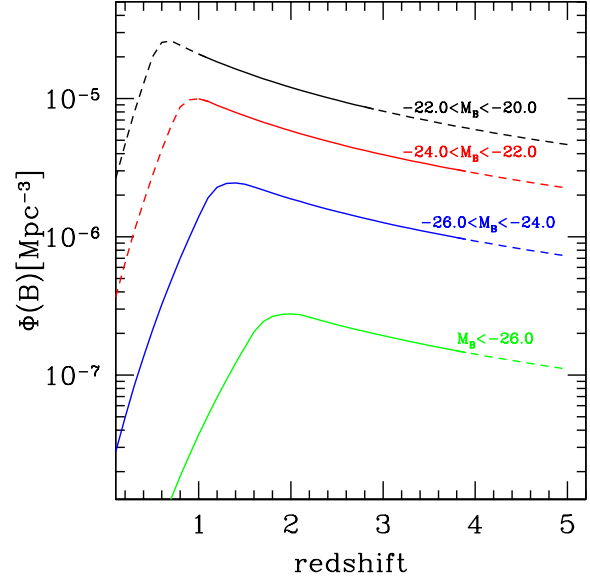


Figure 10. Evolution of comoving AGN space density with redshift, for different luminosity range: $-22.0 < M_B < -20.0$; $-24.0 < M_B < -22.0$; $-26.0 < M_B < -24.0$ and $M_B < -26.0$. Dashed lines correspond to the redshift range in which the model has been extrapolated.

9 and the best fit parameters derived for this model are reported in the last line of Table 2.

This model reproduces well the overall shape of the luminosity function over the entire redshift range, including the excess of faint AGN at $1.0 < z < 1.5$. The χ^2 value for the LDDE model is in fact the best among all the analyzed models. We found in fact a χ^2 of 64.6 for 67 degree of freedom and, as the reduced χ^2 is below 1, it is acceptable⁴.

The best fit value of the faint end slope, which in this model corresponds to the slope at $z = 0$, is $\beta = -2.0$. This value is consistent with that derived by Hao et al. (2005) studying the emission line luminosity function of a sample of Seyfert galaxies at very low redshift ($0 < z < 0.15$), extracted from the SDSS. They in fact derived a slope β ranging from -2.07 to -2.03 , depending on the line ($H\alpha$, $[O\text{II}]$ or $[O\text{III}]$) used to compute the nuclear luminosity. Moreover, also the normalizations are in good agreement, confirming our model also in a redshift range where data are not available and indeed leading us to have a good confidence on the extrapolation of the derived model.

8. The AGN activity as a function of redshift

By integrating the luminosity function corresponding to our best fit model (i.e the LDDE model; see Table 2), we derived the comoving AGN space density as a function of redshift for different luminosity ranges (Figure 10).

The existence of a peak at $z \sim 2$ in the space density of bright AGN is known since a long time, even if rarely it has been possible to precisely locate the position of this maximum within a single optical survey. Figure 10 shows that for our best fit model the peak of the AGN space density shifts significantly towards lower

⁴ We note that the reduced χ^2 of our best fit model, which includes also VVDS data, is significantly better than that obtained by Richards et al. (2006b) in fitting only the SDSS DR3 data.

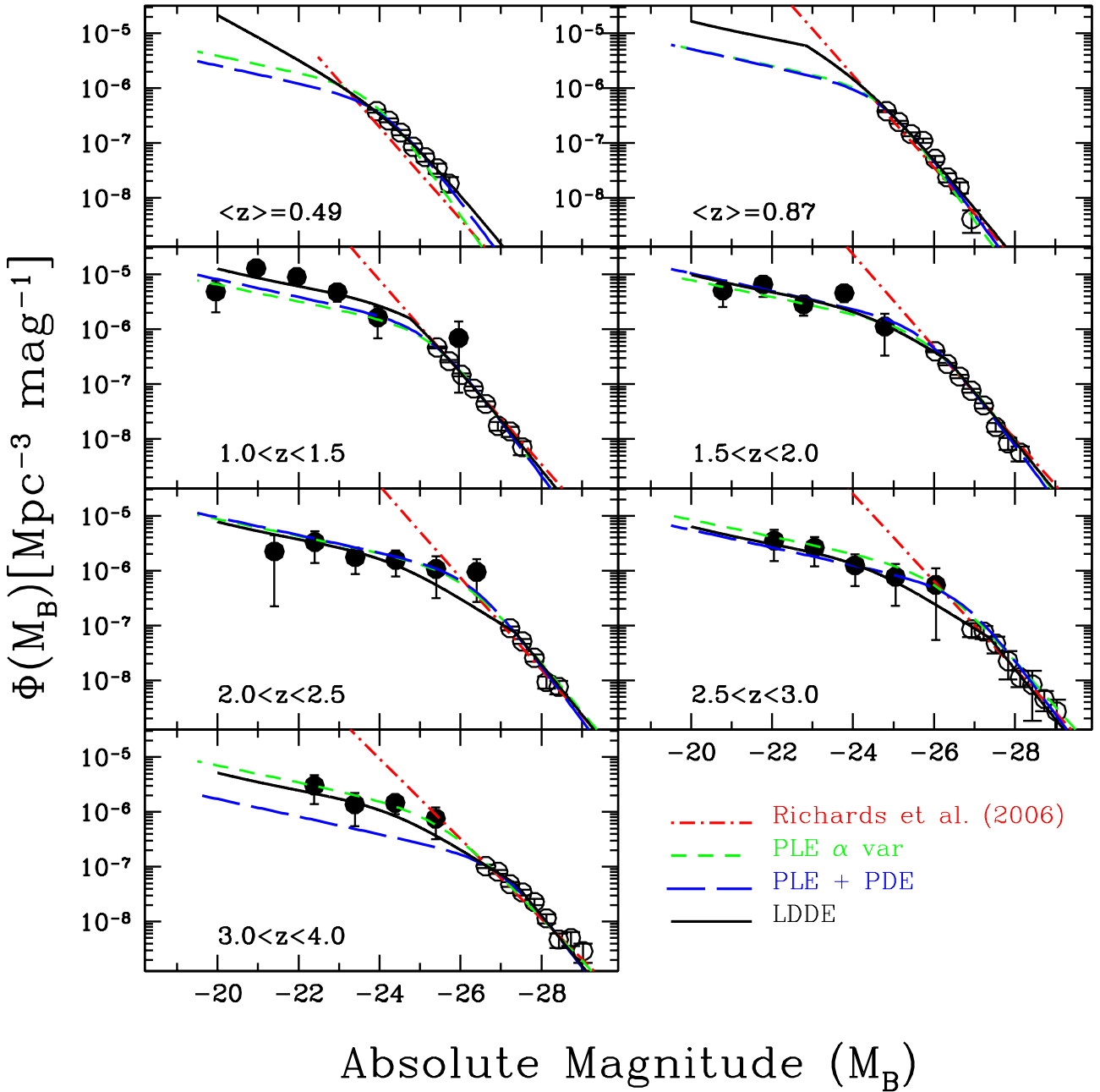


Figure 9. Filled circles correspond to our rest-frame B-band luminosity function data points, derived in the redshift bins $1.0 < z < 1.5$, $1.5 < z < 2.0$, $2.0 < z < 2.5$, $2.5 < z < 3.0$ and $3.0 < z < 4.0$. Open circles are the data points from the SDSS Data Release 3 (DR3) by Richards et al. (2006b). These data are shown also in two redshift bins below $z = 1$. The red dot-dashed line corresponds to the model fit derived by Richards et al. (2006b) only for the SDSS data. The other lines correspond to model fits derived considering the combination of the VVDS and SDSS samples for different evolutionary models, as listed in Table 2 and described in Section 7.

redshift going to lower luminosity. The position of the maximum moves from $z \sim 2.0$ for $M_B < -26.0$ to $z \sim 0.65$ for $-22 < M_B < -20$.

A similar trend has recently been found by the analysis of several deep X-ray selected samples (Cowie et al., 2003; Hasinger et al., 2005; La Franca et al., 2005). To compare with X-ray results, by applying the same bolometric corrections used in Section 6, we derived the volume densities derived by our best fit LDDE model in the same luminosity ranges as La Franca et al. (2005). We found that the volume density

peaks at $z \approx [0.35; 0.7; 1.1; 1.5]$ respectively for $\text{Log}L_{X(2-10\text{keV})} = [42-43; 43-44; 44-44.5; 44.5-45]$. In the same luminosity intervals, the values for the redshift of the peak obtained by La Franca et al. (2005) are $z \approx [0.5; 0.8; 1.1; 1.5]$, in good agreement with our result. This trend has been interpreted as evidence of AGN (i.e. black hole) “cosmic downsizing”, similar to what has recently been observed in the galaxy spheroid population (Cimatti et al., 2006). The downsizing (Cowie et al., 1996) is a term which is used to describe the phenomenon whereby lumi-

1.0 < z < 1.5						1.5 < z < 2.0					
ΔM	N_{qso}	Log $\Phi(B)$	Δ Log $\Phi(B)$			ΔM	N_{qso}	Log $\Phi(B)$	Δ Log $\Phi(B)$		
-19.46	-20.46	3	-5.31	+0.20	-0.38	-20.28	-21.28	4	-5.29	+0.18	-0.30
-20.46	-21.46	11	-4.89	+0.12	-0.16	-21.28	-22.28	7	-5.18	+0.15	-0.22
-21.46	-22.46	17	-5.04	+0.09	-0.12	-22.28	-23.28	7	-5.54	+0.14	-0.20
-22.46	-23.46	9	-5.32	+0.13	-0.18	-23.28	-24.28	10	-5.34	+0.12	-0.17
-23.46	-24.46	3	-5.78	+0.20	-0.38	-24.28	-25.28	2	-5.94	+0.23	-0.53
-25.46	-26.46	1	-6.16	+0.52	-0.76						
2.0 < z < 2.5						2.5 < z < 3.0					
ΔM	N_{qso}	Log $\Phi(B)$	Δ Log $\Phi(B)$			ΔM	N_{qso}	Log $\Phi(B)$	Δ Log $\Phi(B)$		
-20.90	-21.90	1	-5.65	+0.52	-0.76	-21.55	-22.55	3	-5.45	+0.20	-0.38
-21.90	-22.90	3	-5.48	+0.20	-0.38	-22.55	-23.55	4	-5.58	+0.19	-0.34
-22.90	-23.90	4	-5.76	+0.18	-0.30	-23.55	-24.55	3	-5.90	+0.20	-0.38
-23.90	-24.90	4	-5.81	+0.18	-0.30	-24.55	-25.55	2	-6.11	+0.23	-0.53
-24.90	-25.90	2	-5.97	+0.23	-0.53	-25.55	-26.55	1	-6.26	+0.52	-0.76
-25.90	-26.90	2	-6.03	+0.23	-0.55						
3.0 < z < 4.0											
ΔM	N_{qso}	Log $\Phi(B)$	Δ Log $\Phi(B)$								
-21.89	-22.89	4	-5.52	+0.19	-0.34						
-22.89	-23.89	3	-5.86	+0.20	-0.40						
-23.89	-24.89	7	-5.83	+0.14	-0.21						
-24.89	-25.89	3	-6.12	+0.20	-0.38						

Table 1. Binned luminosity function estimate for $\Omega_m=0.3$, $\Omega_\Lambda=0.7$ and $H_0=70 \text{ km} \cdot \text{s}^{-1} \cdot \text{Mpc}^{-1}$. We list the values of Log Φ and the corresponding 1σ errors in five redshift ranges, as plotted with full circles in Figure 9 and in $\Delta M_B=1.0$ magnitude bins. We also list the number of AGN contributing to the luminosity function estimate in each bin

Sample - Evolution Model	α	β	M^*	k_{1L}	k_{2L}	A	k_{1D}	k_{2D}	Φ^*	χ^2	ν
VVDS+SDSS - PLE α var	-3.83	-1.38	-22.51	1.23	-0.26	0.26	-	-	9.78E-7	130.36	69
VVDS+SDSS - PLE+PDE	-3.49	-1.40	-23.40	0.68	-0.073	-	-0.97	-0.31	2.15E-7	91.4	68
Sample - Evolution Model	α	β	M^*	$p1$	$p2$	γ	$z_{c,0}$	M_c	Φ^*	χ^2	ν
VVDS+SDSS - LDDE	-3.29	-2.0	-24.38	6.54	-1.37	0.21	2.08	-27.36	2.79E-8	64.6	67

Table 2. Best fit models derived from the χ^2 analysis of the combined sample VVDS+SDSS-DR3 in the redshift range $0.0 < z < 4.0$ assuming a flat ($\Omega_m + \Omega_\Lambda = 1$) universe with $\Omega_m = 0.3$.

nous activity (star formation and accretion onto black holes) appears to be occurring predominantly in progressively lower mass objects (galaxies or BHs) as the redshift decreases. As such, it explains why the number of bright sources peaks at higher redshift than the number of faint sources.

As already said, this effect had not been seen so far in the analysis of optically selected samples. This can be due to the fact that most of the optical samples, because of their limiting magnitudes, do not reach luminosities where the difference in the location of the peak becomes evident. The COMBO-17 sample (Wolf et al., 2003), for example, even if it covers enough redshift range ($1.2 < z < 4.8$) to enclose the peak of the AGN activity, does not probe luminosities faint enough to find a significant indication for a difference between the space density peaks of AGN of different luminosities (see, for example, Figure 11 in Wolf et al. (2003), which is analogous to our Figure 10, but in which only AGN brighter than $M \sim -24$ are shown). The VVDS sample, being about one magnitude fainter than the COMBO-17 sample and not having any bias in finding faint AGN, allows us to detect for the first time in an optically selected sample the shift of the maximum space density towards lower redshift for low luminosity AGN.

9. Summary and conclusion

In the present paper we have used the new sample of AGN, collected by the VVDS and presented in Gavignaud et al. (2006), to derive the optical luminosity function of faint type-1 AGN.

The sample consists of 130 broad line AGN (BLAGN) selected on the basis of only their spectral features, with no morphological and/or color selection biases. The absence of these biases is particularly important for this sample because the typical non-thermal AGN continuum can be significantly masked by the emission of the host galaxy at the low intrinsic luminosity of the VVDS AGN. This makes the optical selection of the faint AGN candidates very difficult using the standard color and morphological criteria. Only spectroscopic surveys without any pre-selection can therefore be considered complete in this luminosity range.

Because of the absence of morphological and color selection, our sample shows redder colors than those expected, for example, on the basis of the color track derived from the SDSS composite spectrum and the difference is stronger for the intrinsically faintest objects. Thanks to the extended multi-wavelength coverage in the deep VVDS fields in which we have, in addition

to the optical VVDS bands, also photometric data from GALEX, CFHTLS, UKIDSS and SWIRE, we examined the spectral energy distribution of each object and we fitted it with a combination of AGN and galaxy emission, allowing also for the possibility of extinction of the AGN flux. We found that both effects (presence of dust and contamination from the host galaxy) are likely to be responsible for this reddening, even if it is not possible to exclude that faint AGN are intrinsically redder than the brighter ones.

We derived the luminosity function in the B-band for $1 < z < 3.6$, using the usual $1/V_{max}$ estimator (Schmidt, 1968), which gives the space density contributions of individual objects. Moreover, using the prescriptions recently derived by Hopkins et al. (2007), we computed also the bolometric luminosity function for our sample. This allows us to compare our results also with other samples selected from different bands.

Our data, more than one magnitude fainter than previous optical surveys, allow us to constrain the faint part of the luminosity function up to high redshift. A comparison of our data with the 2dF sample at low redshift ($1 < z < 2.1$) shows that the VVDS data can not be well fitted with the PLE models derived by previous samples. Qualitatively, our data suggest the presence of an excess of faint objects at low redshift ($1.0 < z < 1.5$) with respect to these models.

Recently, a growing number of observations at different redshifts, in soft and hard X-ray bands, have found in fact evidences of a similar trend and they have been reproduced with a luminosity-dependent density evolution parameterization. Such a parameterization allows the redshift of the AGN density peak to change as a function of luminosity and explains the excess of faint AGN that we found at $1.0 < z < 1.5$. Indeed, by combining our faint VVDS sample with the large sample of bright AGN extracted from the SDSS DR3 (Richards et al., 2006b), we found that the evolutionary model which better represents the combined luminosity functions, over a wide range of redshift and luminosity, is an LDDE model, similar to those derived from the major X-surveys. The derived faint end slope at $z=0$ is $\beta = -2.0$, consistent with the value derived by Hao et al. (2005) studying the emission line luminosity function of a sample of Seyfert galaxies at very low redshift.

A feature intrinsic to these LDDE models is that the comoving AGN space density shows a shift of the peak with luminosity, in the sense that more luminous AGN peak earlier in the history of the Universe (i.e. at higher redshift), while the density of low luminosity ones reaches its maximum later (i.e. at lower redshift). In particular, in our best fit LDDE model the peak of the space density ranges from $z \sim 2$ for $M_B < -26$ to $z \sim 0.65$ for $-22 < M_B < -20$. This effect had not been seen so far in the analysis of optically selected samples, probably because most of the optical samples do not sample in a complete way the faintest luminosities, where the difference in the location of the peak becomes evident.

Although the results here presented appear to be already robust, the larger AGN sample we will have at the end of the still on-going VVDS survey (> 300 AGN), will allow a better statistical analysis and a better estimate of the parameters of the evolutionary model.

Acknowledgements. This research has been developed within the framework of the VVDS consortium.

This work has been partially supported by the CNRS-INSU and its Programme National de Cosmologie (France), and by Italian Ministry (MIUR) grants COFIN2000 (MM02037133) and COFIN2003 (num.2003020150).

Based on data obtained with the European Southern Observatory Very Large Telescope, Paranal, Chile, program 070.A-9007(A), 272.A-5047, 076.A-0808, and on data obtained at the Canada-France-Hawaii Telescope, operated by the

CNRS of France, CNRC in Canada, and the University of Hawaii. The VLT-VIMOS observations have been carried out on guaranteed time (GTO) allocated by the European Southern Observatory (ESO) to the VIRMOS consortium, under a contractual agreement between the Centre National de la Recherche Scientifique of France, heading a consortium of French and Italian institutes, and ESO, to design, manufacture and test the VIMOS instrument.

References

- Arnouts, S., Schiminovich, D., Ilbert, O., et al. 2005, *ApJ*, 619, L43
 Avni, Y. & Bahcall, J. N. 1980, *ApJ*, 235, 694A
 Barger, A. J., Cowie, L. L., Mushotzky, R. F., et al. 2005, *AJ*, 129, 578
 Boyle, B. J., Shanks, T., Croom, S. M., et al. 2000, *MNRAS*, 317, 1014
 Boyle, B. J., Shanks, T., & Peterson, B. A. 1988, *MNRAS*, 235, 935
 Brandt, W. N., Hornschemeier, A. E., Schneider, D. P., et al. 2000, *AJ*, 119, 2349
 Brown, M. J. I., Brand, K., Dey, A., et al. 2006, *ApJ*, 638, 88
 Bruzual, G. & Charlot, S. 2003, *MNRAS*, 344, 1000
 Cimatti, A., Daddi, E., & Renzini, A. 2006, *A&A*, 453, L29
 Cirasuolo, M., Magliocchetti, M., & Celotti, A. 2005, *MNRAS*, 357, 1267
 Cowie, L. L., Barger, A. J., Bautz, M. W., Brandt, W. N., & Garmire, G. P. 2003, *ApJ*, 584, L57
 Cowie, L. L., Songaila, A., Hu, E. M., & Cohen, J. G. 1996, *AJ*, 112, 839
 Croom, S. M., Smith, R. J., Boyle, B. J., et al. 2004, *MNRAS*, 349, 1397
 Di Matteo, T., Springel, V., & Hernquist, L. 2005, *Nature*, 433, 604
 Fan, X., Strauss, M. A., Schneider, D. P., et al. 2001, *AJ*, 121, 54
 Ferrarese, L. & Merritt, D. 2000, *ApJ*, 539, L9
 Fiore, F., Brusa, M., Cocchia, F., et al. 2003, *A&A*, 409, 79
 Fontanot, F., Cristiani, S., Monaco, P., et al. 2007, *A&A*, 461, 39
 Gavignaud, I., Bongiorno, A., Paltani, S., et al. 2006, *ArXiv Astrophysics e-prints*
 Hall, P. B., Gallagher, S. C., Richards, G. T., et al. 2006, *AJ*, 132, 1977
 Hao, L., Strauss, M. A., Fan, X., et al. 2005, *AJ*, 129, 1795
 Hartwick, F. D. A. & Schade, D. 1990, *ARA&A*, 28, 437
 Hasinger, G., Miyaji, T., & Schmidt, M. 2005, *A&A*, 441, 417
 Hewett, P. C. & Foltz, C. B. 2003, *AJ*, 125, 1784
 Hewett, P. C., Foltz, C. B., Chaffee, F. H., et al. 1991, *AJ*, 101, 1121
 Hopkins, P. F., Hernquist, L., Cox, T. J., et al. 2006, *ApJ*, 639, 700
 Hopkins, P. F., Richards, G. T., & Hernquist, L. 2007, *ApJ*, 654, 731
 Hunt, M. P., Steidel, C. C., Adelberger, K. L., & Shapley, A. E. 2004, *ApJ*, 605, 625
 Ilbert, O., Tresse, L., Zucca, E., et al. 2005, *A&A*, 439, 863
 Iovino, A., McCracken, H. J., Garilli, B., et al. 2005, *A&A*, 442, 423
 Kennefick, J. D., Djorgovski, S. G., & de Carvalho, R. R. 1995, *AJ*, 110, 2553
 Kormendy, J. & Richstone, D. 1995, *ARA&A*, 33, 581
 La Franca, F., Fiore, F., Comastri, A., et al. 2005, *ApJ*, 635, 864
 La Franca, F., Fiore, F., Vignali, C., et al. 2002, *ApJ*, 570, 100
 Lawrence, A., Warren, S. J., Almaini, O., et al. 2006, *ArXiv Astrophysics e-prints*
 Le Fèvre, O., Mellier, Y., McCracken, H. J., et al. 2004a, *A&A*, 417, 839
 Le Fèvre, O., Vettolani, G., Paltani, S., et al. 2004b, *A&A*, 428, 1043
 Le Fèvre, O., Vettolani, G., Garilli, B., et al. 2005, *A&A*, 439, 845
 Lonsdale, C., Polletta, M. d. C., Surace, J., et al. 2004, *ApJS*, 154, 54
 Lonsdale, C. J., Smith, H. E., Rowan-Robinson, M., et al. 2003, *PASP*, 115, 897
 Magorrian, J., Tremaine, S., Richstone, D., et al. 1998, *AJ*, 115, 2285
 Marshall, H. L., Tananbaum, H., Avni, Y., & Zamorani, G. 1983, *ApJ*, 269, 35
 Matute, I., La Franca, F., Pozzi, F., et al. 2006, *A&A*, 451, 443
 McCracken, H. J., Radovich, M., Bertin, E., et al. 2003, *A&A*, 410, 17
 Miyaji, T., Hasinger, G., & Schmidt, M. 2000, *A&A*, 353, 25
 Miyaji, T., Hasinger, G., & Schmidt, M. 2001, *A&A*, 369, 49
 Mushotzky, R. F., Cowie, L. L., Barger, A. J., & Arnaud, K. A. 2000, *Nature*, 404, 459
 Osterbrock, D. E. 1981, *ApJ*, 249, 462
 Page, M. J., Mason, K. O., McHardy, I. M., Jones, L. R., & Carrera, F. J. 1997, *MNRAS*, 291, 324
 Pei, Y. C. 1995, *ApJ*, 438, 623
 Prevot, M. L., Lequeux, J., Prevot, L., Maurice, E., & Rocca-Volmerange, B. 1984, *A&A*, 132, 389
 Radovich, M., Arnaboldi, M., Ripepi, V., et al. 2004, *A&A*, 417, 51
 Richards, G. T., Croom, S. M., Anderson, S. F., et al. 2005, *MNRAS*, 360, 839
 Richards, G. T., Fan, X., Newberg, H. J., et al. 2002, *AJ*, 123, 2945
 Richards, G. T., Hall, P. B., Vanden Berk, D. E., et al. 2003, *AJ*, 126, 1131
 Richards, G. T., Lacy, M., Storrie-Lombardi, L. J., et al. 2006a, *ApJS*, 166, 470
 Richards, G. T., Strauss, M. A., Fan, X., et al. 2006b, *AJ*, 131, 2766
 Scannapieco, E. & Oh, S. P. 2004, *ApJ*, 608, 62
 Schiminovich, D., Ilbert, O., Arnouts, S., et al. 2005, *ApJ*, 619, L47
 Schlegel, D. J., Finkbeiner, D. P., & Davis, M. 1998, *ApJ*, 500, 525
 Schmidt, M. 1968, *ApJ*, 151, 393

Schmidt, M., Schneider, D. P., & Gunn, J. E. 1995, *AJ*, 110, 68
 Schneider, D. P., Fan, X., Hall, P. B., et al. 2003, *AJ*, 126, 2579
 Siana, B., Polletta, M., Smith, H. E., et al. 2006, *ArXiv Astrophysics e-prints*
 Silk, J. & Rees, M. J. 1998, *A&A*, 331, L1
 Silverman, J. D., Green, P. J., Barkhouse, W. A., et al. 2005, *ApJ*, 624, 630
 Steidel, C. C., Hunt, M. P., Shapley, A. E., et al. 2002, *ApJ*, 576, 653
 Ueda, Y., Akiyama, M., Ohta, K., & Miyaji, T. 2003, *ApJ*, 598, 886
 Vanden Berk, D. E., Richards, G. T., Bauer, A., et al. 2001, *AJ*, 122, 549
 Warren, S. J., Hewett, P. C., & Osmer, P. S. 1994, *ApJ*, 421, 412
 Wolf, C., Wisotzki, L., Borch, A., et al. 2003, *A&A*, 408, 499

¹ Università di Bologna, Dipartimento di Astronomia - Via Ranzani 1, I-40127, Bologna, Italy

² INAF-Osservatorio Astronomico di Bologna - Via Ranzani 1, I-40127, Bologna, Italy

³ Astrophysical Institute Potsdam, An der Sternwarte 16, D-14482 Potsdam, Germany

⁴ Integral Science Data Centre, ch. d'Écogia 16, CH-1290 Versoix

⁵ Geneva Observatory, ch. des Maillettes 51, CH-1290 Sauverny, Switzerland

⁶ Laboratoire d'Astrophysique de Toulouse/Tabres (UMR5572), CNRS, Université Paul Sabatier - Toulouse III, Observatoire Midi-Pyrénées, 14 av. E. Belin, F-31400 Toulouse, France

⁷ Institute for Astronomy, University of Edinburgh, Royal Observatory, Edinburgh EH9 3HJ

⁸ IASF-INAF - via Bassini 15, I-20133, Milano, Italy

⁹ Laboratoire d'Astrophysique de Marseille, UMR 6110 CNRS-Université de Provence, BP8, 13376 Marseille Cedex 12, France

¹⁰ IRA-INAF - Via Gobetti, 101, I-40129, Bologna, Italy

¹¹ INAF-Osservatorio Astronomico di Roma - Via di Frascati 33, I-00040, Monte Porzio Catone, Italy

¹² Max Planck Institut für Astrophysik, 85741, Garching, Germany

¹³ Institut d'Astrophysique de Paris, UMR 7095, 98 bis Bvd Arago, 75014 Paris, France

¹⁴ School of Physics & Astronomy, University of Nottingham, University Park, Nottingham, NG72RD, UK

¹⁵ INAF-Osservatorio Astronomico di Brera - Via Brera 28, Milan, Italy

¹⁶ Institute for Astronomy, 2680 Woodlawn Dr., University of Hawaii, Honolulu, Hawaii, 96822

¹⁷ Observatoire de Paris, LERMA, 61 Avenue de l'Observatoire, 75014 Paris, France

¹⁸ Centre de Physique Théorique, UMR 6207 CNRS-Université de Provence, F-13288 Marseille France

¹⁹ Astronomical Observatory of the Jagiellonian University, ul. Orła 171, 30-244 Kraków, Poland

²⁰ INAF-Osservatorio Astronomico di Capodimonte - Via Moiariello 16, I-80131, Napoli, Italy

²¹ Instituto de Astrofísica de Canarias, C/ Via Lactea s/n, E-38200 La Laguna, Spain

²² Center for Astrophysics & Space Sciences, University of California, San Diego, La Jolla, CA 92093-0424, USA

²³ Centro de Astrofísica da Universidade do Porto, Rua das Estrelas, 4150-762 Porto, Portugal

²⁴ Università di Milano-Bicocca, Dipartimento di Fisica - Piazza delle Scienze 3, I-20126 Milano, Italy

²⁵ Università di Bologna, Dipartimento di Fisica - Via Irnerio 46, I-40126, Bologna, Italy